A Numerical Study of the Sensitivity of Typhoon Track and Convection Structure to Cloud Microphysics

Li-Huan Hsu[1] , Shih-Hao Su[2] , and Hung-Chi Kuo[3]

[1]National Science and Technology Center for Disaster Reduction, New Taipei City, Taiwan, [2]Department of Atmospheric Sciences, Chinese Culture University, Taipei, Taiwan, [3]Department of Atmospheric Sciences, National Taiwan University, Taipei, Taiwan

Abstract Typhoon Saola affected Taiwan from July 30, 2012, to August 03, 2012. It started in a northwestward track, and it was weakening to Category 1 storm and had a sharp cyclonic deflection track when it was about to made landfall in Taiwan on August 02. After the deflection, the typhoon moved northward and then northwestward across northern Taiwan. The cyclonic southward deflection and the northward motion constituted 12 h of looping motion which increase both the typhoon duration time and the rainfall in northeastern Taiwan. This research is to study the looping motion by the Weather Research and Forecasting model for this very weak typhoon. The model is able to reproduce the looping motion similar to that of observation. The model shows a strong asymmetry of precipitation and cross-mountain downslope wind near the typhoon center while the typhoon track is looping toward the southwest. The potential vorticity (PV) tendency diagnosis confirms that diabatic heating and downslope wind vertical stretching are the major contributors to tropical cyclone southwestward motion, rather than the commonly referred channeling effect. The asymmetric rainfall disappears when the tropical cyclone starts moving northward in its end-stage of looping. The northward motion is dominated by horizontal advection of PV tendency. The results highlight the influence of convection and downslope wind near steep terrain on the initial southward motion in the looping track. The model sensitivity study indicates that a large part of track uncertainty resides in the interaction of model internal dynamics and model cloud microphysics.

Plain Language Summary Typhoon Saola, a weak Category one storm, affected Taiwan from July 30, 2012, to August 03, 2012. This northwestward moving typhoon experience a sharp cyclonic deflection motion when it was about to made landfall, and then move northwestward across northern Taiwan. The cyclonic southward deflection and the northward motion constituted 12 h of looping motion which increase both the typhoon duration time and the rainfall in northeastern Taiwan. Our numerical simulation reproduces the looping motion similar to that of observation. The model simulates, in general agreement with the observations, a strong asymmetry of precipitation and cross-mountain downslope wind near the typhoon center while the typhoon track is looping toward the southwest. The asymmetric rainfall disappears when the tropical cyclone starts moving northward in its end-stage of looping. We demonstrate that diabatic heating and downslope wind vertical stretching are the major contributors to tropical cyclone southwestward motion, rather than the commonly referred channeling effect. The horizontal advection of potential vorticity tendency then dominates for the northward motion in the end-stage. The model sensitivity experiments indicate that a large part of track uncertainty resides in the interaction of model internal dynamics and model cloud microphysics.

1. Introduction

Typhoon Saola (2012) formed as a tropical depression at 13.6°N, 127.3°E on July 27, 2012, and intensified to a tropical cyclone (TC) within a day. The Joint Typhoon Warning Center (JTWC) named it Typhoon Saola (2012) at 06 UTC on July 28. It strengthened to a Category 2 typhoon at 00 UTC August 01 and weakened again to Category 1 on the same day. Figure 1 shows the lifetime trajectory of Typhoon Saola (2012). The TC moved toward the northwest after it formed and affected Taiwan from July 30 to August 03. It deflected cyclonically while approaching Taiwan, made a loop, and turned back to the northwestward path after August 02. Several TCs have occurred in the past that had similar "cyclonic looping" tracks, including Typhoon Polly (1992), Typhoon Haitang (2005), Typhoon Krosa (2007), and Typhoon Sinlaku (2008). Most of the
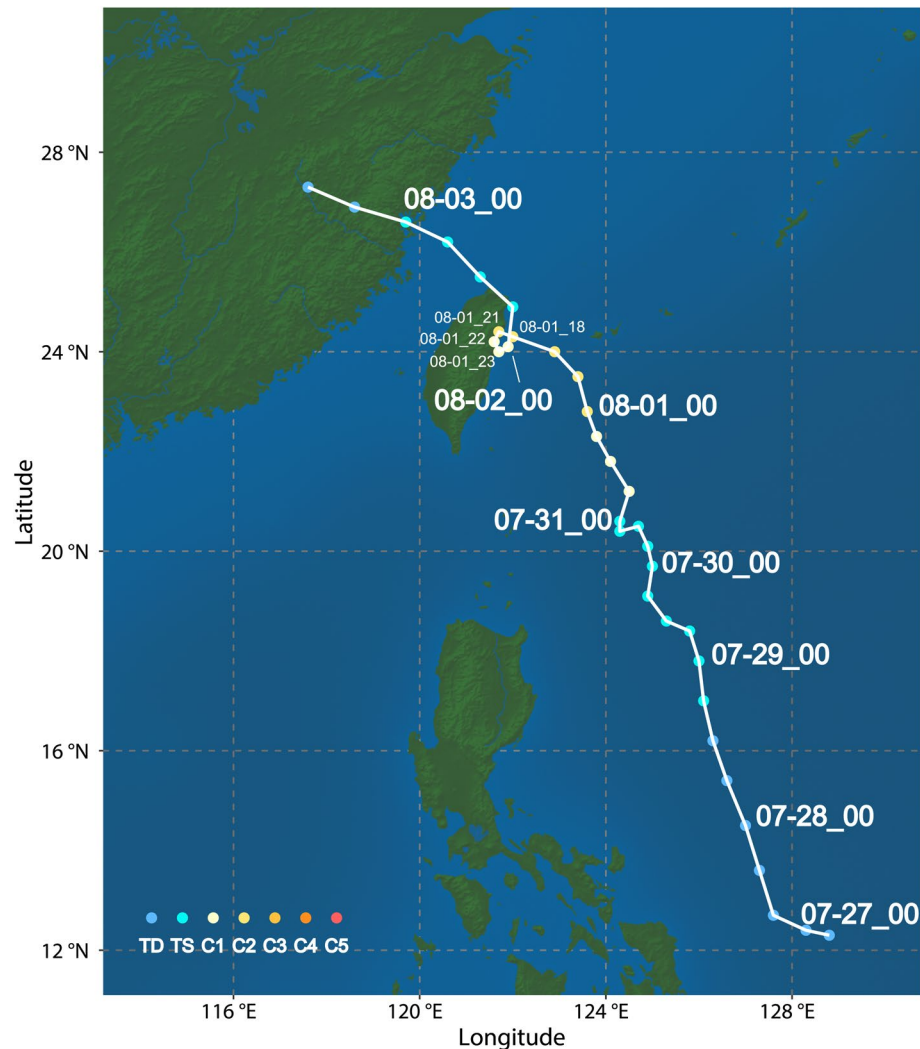
Figure 1. Lifetime trajectory of typhoon Saola (2012) by Joint Typhoon Warning Center best track. The color code shows the intensity (Saffir-Simpson Hurricane Wind Scale) of tropical cyclone.

typhoons mentioned are strong storms of Cat.3 or above. Forty-nine out of 84 landfalling TCs have this kind of deflection track from 1960 to 2010, and only seven of them have complete looping motions (see Figure 1 and Table 1 of Hsu et al., 2018). The translation speeds of typhoons with a looping track before making landfall are usually slower than those of other typhoons (Hsu et al., 2018). Su et al. (2012) reported that this type of looping motion could lengthen the duration and lead to extreme rainfall before typhoons make landfall. An interesting feature to note is that Typhoon Soala (2012) is the weakest in intensity and possesses a pronounced looping track.

Typhoon track deflections can be caused by interactions between typhoon circulation and Taiwan topography through several mechanisms. For example, the blocking effect (Lin et al., 1999, 2005) or the channeling effect (Huang et al., 2011; Jian & Wu, 2008; Wu et al., 2015; Yeh & Elsberry, 1993) can alter the wind flow between typhoon and topography, producing an asymmetric near-shore southward deflection of the TC motion. The advection flow vectors, according to the model simulations, then rotate cyclonically to cause the looping track. The underlying mechanism of such a rotation, however, has not been studied comprehensively. Moreover, if the channeling effect is to dominate the looping, the looping tracks would occur in the central or southern part of the east coast as the CMR is much higher in the central part of the east coast. The typhoon cases studied for the channeling effect are most of the strong typhoon types. For example, the channeling effect in the Super typhoon Haitang (2015) was studied by Jian and Wu (2008). The channeling

effect may not be pronounced in a weak storm. Yeh et al. (2012) revealed that the secondary vortex induced by the typhoon and Taiwan topography can also contribute to a looping track of Typhoon Haitang (2015). Huang and Lin (2018) conducted a series of idealized numerical experiments by using a dry and hydrostatic fluid to explore crucial nondimensional parameters for typhoons with a looping track. They showed the typhoons with a looping track that favors the conditions of the slow movement, strong orographic blocking, and strong TC vortex.

Topographic vorticity stretching by the cross-mountain flow is another mechanism that affects the motion of the approaching vortex other than blocking and channeling (Kuo et al., 2001). The other way of generating the asymmetric vorticity or PV thus affects the typhoon motion through the diabatic heating effect (Fovell et al., 2009, 2010, 2016; Fovell & Su, 2007). Fovell and Su (2007) used idealized model simulations to show that the sensitivity of the convection process is non-negligible and can cause a huge divergence on typhoon track forecasts with different cumulus schemes or cloud microphysics processes. On the other hand, Hsu et al. (2013, 2018) showed the asymmetric convection that phased locked with the CMR and wavenumber-1 (WN1) component significantly affects the typhoon translation speed and direction. Previous studies, such as Chen et al. (2017), Tang and Chan (2014, 2015, 2016), and Wang et al. (2012, 2013) also studied the similar effect of asymmetric convection induced by the Taiwan topography. It has been discussed in many studies that the vorticity budget analysis or the potential vorticity (PV) tendency diagnosis is a useful diagnosis to explain the model results (Hsu et al., 2018; Huang & Lin, 2008; Lin et al., 2016; Lin & Savage, 2011; Liu et al., 2016).

As Typhoon Saola (2012) approached the terrain, despite it is a Cat. 1 weak storm, the composite radar reflectivity also showed significant asymmetric convection structures (Figure 2). The convection on the windward side to the north of the storm and the very weak convection zone to the south of the storm are clearly seen during the period of storm southward deflection (Figures 2b and 2c). The weak convection zone is caused by subsidence and flow across the CMR. The convection asymmetry to the north of the storm weakens in Figure 2d when the storm is in the last stage of looping with northward motion. Since the storm is of Cat. 1 intensity, the channeling effect may be less contribution for the pronounced southward deflection compared to that of a strong vortex like Typhoon Haitang (2015). It is possible that this asymmetric convection may cause uneven diabatic effects and affect TC movements. This type of TC track variation may occur in less than 6 h but is crucial in determining the TC landfall position and associated rainfall maxima in Taiwan. Understanding the mechanism and variation source of the looping track is conductive to disaster prevention operation. This study examined the mechanism of Typhoon Saola's (2012) looping track near Taiwan. The numerical experiments and PV tendency diagnosis method are described in Section 2. Section 3 discusses the results of simulation experiments and PV tendency diagnosis. The sensitivities of cloud microphysics schemes are discussed in Section 4 and conclusions are drawn in Section 5.

2. Numerical Experiments and Diagnosis Method

2.1. Model Settings

In this study, we use the Weather Research and Forecasting (WRF) model, version 3.8.1 (Skamarock et al., 2008), to simulate Typhoon Saola (2012). We use a single domain centered at 23.23°N, 122.55°E with a horizontal resolution of 3 km (601 × 601 grids). The model top is set at 10 hPa with 41 vertical layers. The 30-arc-second (approximately 1 km) Global Multiresolution Terrain Elevation Data (Danielson & Gesch, 2011) (GMTED2010) is used for model topography in this study. The land-use data come from the 21-class IGBP moderate-resolution imaging spectroradiometer (MODIS) 30-arc-second spatial resolution data set (Friedl et al., 2010). The initial and lateral boundary conditions used in WRF simulations are the 6 hourly, 1° × 1° NCEP Final Analysis (FNL) data from the Global Forecast System (NCEP, 2000). The simulations began at 1800 UTC on July 30, 2012, and ended at 1800 UTC on August 02, 2012, for a total of 72 h with time steps equal to 20 s.

The WRF physics include the Yonsei University planetary boundary layer scheme (Hong et al., 2006), revised MM5 similarity surface-layer scheme (Jiménez et al., 2012), unified Noah land surface model (Tewari et al., 2004), and Rapid Radiative Transfer Model for General Circulation Models longwave and shortwave radiation parameterizations (Iacono et al., 2008). The microphysics in the control run is the Goddard
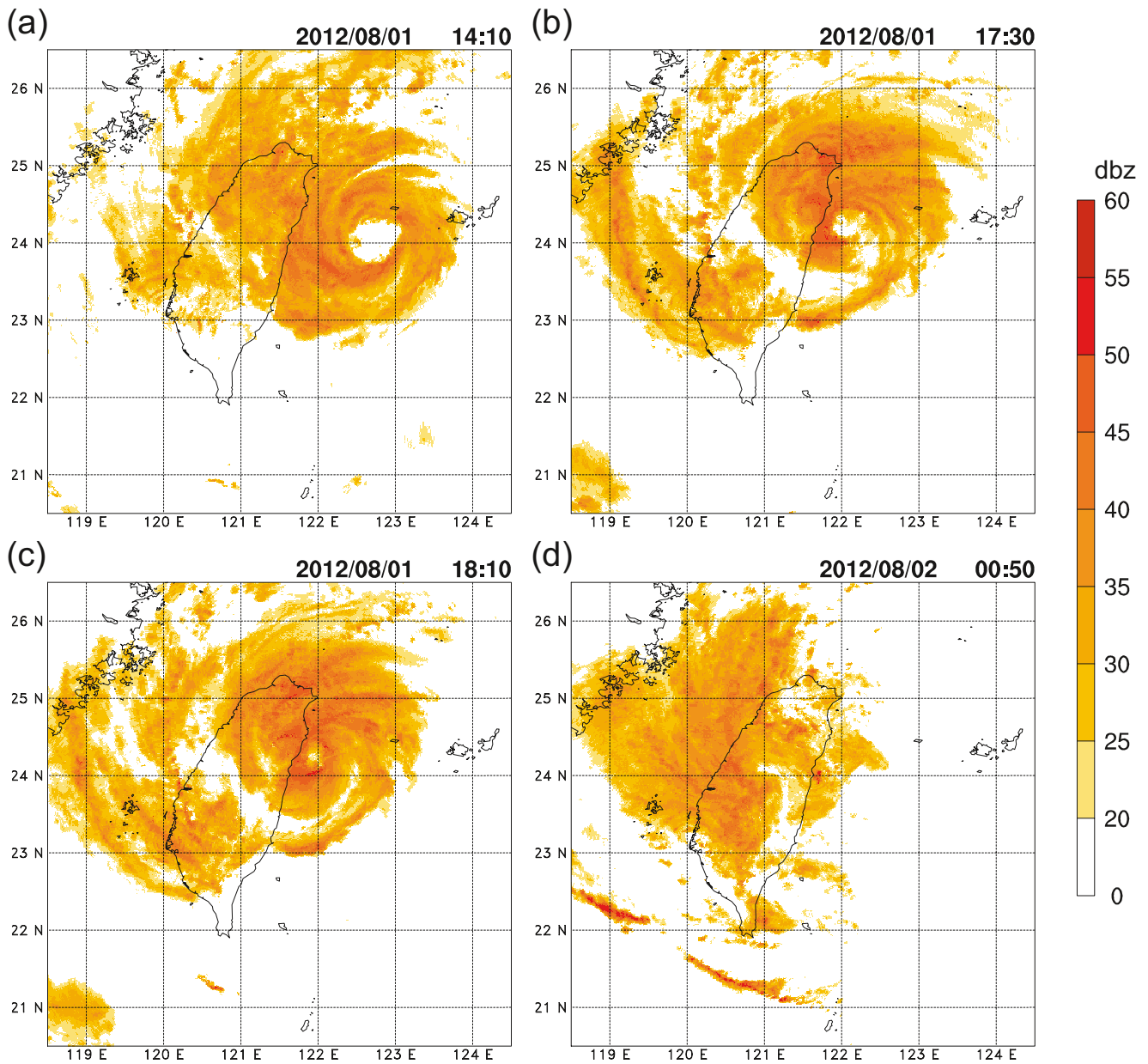
Figure 2. Composite radar reflectivity of Typhoon Saola (2012) from Taiwan Central Weather Bureau's Quantitative Precipitation Estimation and Segregation Using Multiple Sensor (QPESUMS) system at (a) 1410 UTC on August 1, 2012, (b) 1730 UTC on August 1, 2012, (c) 1810 UTC on August 1, 2012, and (d) 0050 UTC on August 2, 2012.

scheme (Tao et al., 1989, 2016). A series of microphysics sensitivity experiments have been conducted using Thompson (Thompson et al., 2008), Morrison (Morrison et al., 2009), WDM6 (Lim & Hong, 2010), WSM6 (Hong & Lim, 2006), and Lin (Chen & Sun, 2002) schemes (Table 1). Among the six microphysics schemes, the Goddard, Lin, and WSM6 schemes are single-moment schemes, and the Thompson, Morrison, and WDM6 schemes are double-moment schemes. The mass of six classes of hydrometers, namely water vapor, cloud water, cloud ice, rain, snow, and graupel, are involved as predictive variables in the Lin scheme. The Goddard scheme has relatively smaller particles for graupel and more large particles for hail. In addition, the saturation condition is different from the Lin scheme. Furthermore, WSM6 is based on the Lin scheme, except that it modulates the ice-phase behavior and sedimentation rate for graupel. The double-moment scheme predicts both the number concentration and the mixing ratio of hydrometers. For example, WDM6 is the double-moment version of WSM6 and also predicts the number concentration of clouds and rain.

Table 1
List of Experiments, Model Settings, and Track Characteristics

Name	Microphysics	Looping	Southward deflection
CTRL	Goddard	Y	Y
THOM	Thompson	N	Y
LIN	Lin	N	Y
WSM6	WSM6	N	Y
MORR	Morrison	N	N
WDM6	WDM6	N	N

The Thompson scheme predicts the number concentration of ice and rain, and the Morrison scheme predicts the number concentration of ice, snow, rain, and graupel.

2.2. Potential Vorticity Tendency Diagnosis

Wu and Wang (2000, 2001) proposed that a storm dominated by its symmetric circulation will move to the maximum in the azimuthal WN1 component of PV tendency in a fixed frame. The storm motion is correlated with the WN1 components as Equation 1.

$$\left(\frac{\partial P}{\partial t} \right)_1 = -C_x \frac{\partial P_s}{\partial x} - C_y \frac{\partial P_s}{\partial y}, \tag{1}$$

Here P is PV and the subscript "s" and "1" denote the symmetric and WN1 components, and C_x and C_y are the scalar speeds in the east and north directions, respectively. The left-hand side of Equation 1 represents the WN1 component of net PV tendency, or the contribution to the WN1 PV tendency from horizontal advection (HA), vertical advection (VA), and diabatic heating (DH) terms, expressed as Equations 2–5.

$$\left(\frac{\partial P}{\partial t} \right)_1 = (HA)_1 + (VA)_1 + (DH)_1, \tag{2}$$

$$HA = \left[-V \cdot \nabla_h P \right], \tag{3}$$

$$VA = \left[-w \frac{\partial P}{\partial z} \right], \tag{4}$$

$$DH = \left[\frac{1}{\rho} \nabla_3 \cdot (Qq) \right], \tag{5}$$

where the [.] denotes the deep layer average over some region centered at the storm, V and w are horizontal and vertical velocities, respectively; ∇_h and ∇_3 are horizontal and three-dimensional gradient operators, respectively; ρ is density; Q is the diabatic heating rate, and q is the three-dimensional absolute vorticity. Wu and Wang (2000, 2001) showed that the scalar speeds C_x and C_y can be determined by applying regressions between the WN1 PV tendencies and symmetric PV gradients in x and y directions, as Equation 6.

$$C_x = -\frac{\sum_{i=1}^{n} \overline{\left(\frac{\partial P_s}{\partial x} \right)_i \left(\frac{\partial P}{\partial t} \right)_{1i}}}{\sum_{i=1}^{n} \overline{\left(\frac{\partial P_s}{\partial x} \right)_i^2}}, \quad C_y = -\frac{\sum_{i=1}^{n} \overline{\left(\frac{\partial P_s}{\partial y} \right)_i \left(\frac{\partial P}{\partial t} \right)_{1i}}}{\sum_{i=1}^{n} \overline{\left(\frac{\partial P_s}{\partial y} \right)_i^2}}, \tag{6}$$

The speeds C_x and C_y thus form a vector representing the magnitude and direction of storm motion or the WN1 contribution to the HA, VA, and DH terms. Notice that the DH term in Equation 5 is usually significant in a TC environment, but Equation 6 implies only the asymmetric part of WN1 that cooperates with the symmetric PV gradient can contribute to the TC motion. The DH contributions to the positive WN1 PV tendency do not necessarily directly point to the rainfall maxima region in the storm. With PV tendency generated by convection, negative (positive) PV anomaly is generated above (below) the heating peak. Thus, the signs and the anomaly magnitude of the deep-layer averaged DH PV tendency depend on the peak height of convection. When the convection peak height is low (high), the vertical averaged PV anomaly may be negative (positive), as is discussed in Hsu et al. (2018). The rainfall maximum region thus may not necessarily be the maximum positive PV anomaly region that contributes to the WN1 PV tendency. Note that Equation 6 implies the storm motion affected by the diabatic heating anomaly and depends on the vortex structure, which can be influenced by the TC-terrain interactions.

The decomposition of PV tendency into symmetric and WN1 parts has been widely used to understand the dynamics and physical processes that contribute directly to the storm motion (Cao et al., 2011; Chen et al., 2017; Fovell et al., 2010, 2016; Hsu et al., 2013, 2018; Huang et al., 2017; Tang & Chan, 2014, 2015; Wu & Wang, 2000, 2001). The validity of the diagnosis method lies in the smallness of the residual term which is defined as the difference between the PV diagnosed track and the model simulated track. Studies have shown that $(HA)_1$, $(VA)_1$, and $(DH)_1$ add up reasonably well to the total WN1 PV tendency, which represents the TC motion (Cao et al., 2011; Fovell et al., 2016; Hsu et al., 2013, 2018). There are, however, limitations of the PV tendency method. The HA, VA, and DH terms can affect each other through the physical disturbance caused by topography and provoke alternation in convection, reflected in DH, that further influence the airflow encountering the terrain (Cao et al., 2011; Hsu et al., 2013, 2018). Thus, the PV diagnosis elucidates the direct WN1 PV contribution to the storm track and the contribution may not necessarily imply a single mechanism in absolute causal effect. In addition, the PV tendency terms can vary with height and time. Hsu et al. (2013, 2018) indicate that deep-layer and temporal averaging over some area covering the storm, in a way similar to the steering flow calculation, can reduce the residual magnitude and thus provides a useful way of demonstrating how the WN1 component of HA, VA, and DH contribute to the model track motion. This study employs this PV tendency diagnosis method to understand the PV contribution to the storm track simulations. The vortex center is determined by the local minimum of 10-m wind circulation near the location of the lowest sea-level pressure. The diagnostic analysis is obtained within a 40,000 km² square horizontal area centered on the TC. Following Hsu et al. (2013, 2018), temporal and vertical averaging is applied to our PV tendency analysis. According to our target storm motions, the PV budget terms are averaged through 6-h and from 600-m to 10-km in height. These criteria are chosen empirically to involve the symmetric and WN1 PV structures of the simulated Typhoon Saola horizontally and vertically.

3. Typhoon Saola (2012) Simulation

3.1. Overview

Figure 3a shows the hourly best track from the Central Weather Bureau (CWB) of Taiwan (red), and the simulated hourly typhoon track (blue) from the control experiment (hereafter, CTRL). The simulated typhoon centers are defined using the local surface wind minimum near the sea-level pressure minimum. Figure 3b shows the time series of TC motion vectors. The simulated TC first moved toward the northwest and started to deflect cyclonically toward Taiwan after 1200 UTC on August 01. It then made a cyclonic loop between 0000 UTC to 0300 UTC on August 02 in the vicinity of Taiwan's northeastern coast (approximately 24°N, 122°E) and then moved northward. The simulated TC finally translated northwestward again after 1200 UTC on August 02 and passed over Taiwan. In general, our CTRL experiment reproduce the southward deflection and the northward motion while approaching Taiwan. The simulated typhoon centers during the southwestward motion period are only approximately 20-km east of the observation centers.

The observed and simulated 72-h (1800 UTC on July 30 to 1800 UTC on August 02, 2012) accumulated rainfall in Taiwan are shown in Figure 4a left and right, respectively. The rainfall maximum exceeds 1,500 mm and occurs in Yilan County, the northeastern of Taiwan. This maximum rainfall has mostly occurred in the windward side while typhoon is deflecting toward the southwest. With the reasonable simulated TC track, the accumulated rainfall maximum and rainfall pattern are in general consistent with the observation, except the southern mountain area. A larger simulated TC may cause massive rainfall in the southern mountain area. Figure 4b shows the comparison of simulated time series minimum sea-level pressure (blue line) with CWB observations. Typhoon Saola (2012) started to intensify at 0000 UTC on August 01, and the minimum sea-level pressure reached 960 hPa from 0600 UTC to 1800 UTC on August 01. The typhoon intensity decreased after 1800 UTC on August 01. The simulated minimum sea-level pressure shows a similar trend, and the maxima intensity exceeds 935 hPa during this period. In general, the simulated TC is stronger than the CWB records.

Figure 5 shows the simulated 3-hourly rainfall and 10-m winds. Four snapshots are chosen manually to represent the rainfall pattern, while TC is in different movement characteristics. TC moves toward the northwest in the beginning, and the rainfall mostly occurs on the left-hand side of the TC movement direction (Figure 5a). The simulated TC starts to deflect cyclonically toward the west at approximately 24°N, 122.7°E. The maximum rainfall appears on the right-hand side of the TC movement direction (Figure 5b).
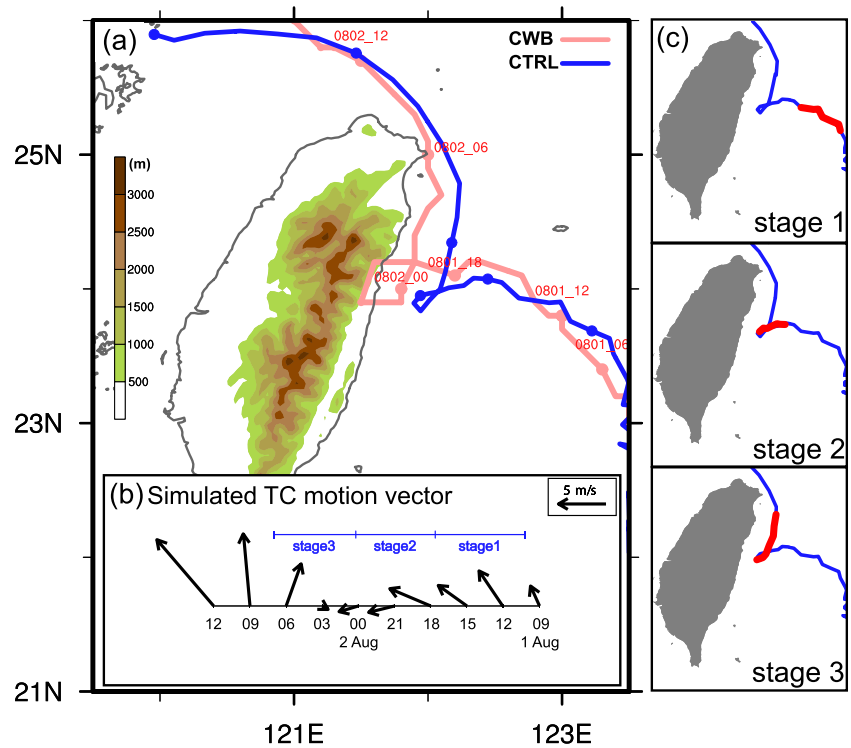
Figure 3. (a) Weather Research and Forecasting control experiment simulated hourly typhoon track (blue line) and Central Weather Bureau hourly best track (red line). Blue dots mark the simulated tropical cyclone (TC) positions every 6 h. (b) Time series of 3-hourly TC motion vectors from control experiment (CTRL). It also labeled the three stages analyzed with the PV tendency diagnosis. (c) Schematic diagrams of the corresponded simulated tracks (red) for three diagnosis stages.

Furthermore, the convection extends to the windward side of northeastern Taiwan. A surface warming area is associated with a local low in the southwest of the TC center (not shown). The cyclonic deflection track as well as the rainfall distribution and surface warming characteristics are in agreement with the idealized experiments conducted by Hsu et al. (2018). The convection in the north of the TC center becomes weak, and the convection pattern becomes more symmetric near the typhoon center while TC is in the stage of looping motion (Figure 5c). TC moves toward the north after the looping motion. The rainfall maximum appears in the west of the TC center during this period (Figure 5d).

The simulated maximum radar reflectivity is shown in Figure 6. Moreover, the simulated maximum radar reflectivity indicates the same asymmetric distribution with the rainfall pattern (Figures 6a and 6b). The radar reflectivity in the north of the TC center becomes stronger while the TC is approaching Taiwan. The distribution of radar reflectivity near the TC center becomes symmetrical when the TC is forming a loop (Figure 6c). After the looping track, a large radar reflectivity occurs in the west of the typhoon center. Overall, the asymmetric pattern is more significant in observations (Figure 2b). A notable weak band of radar reflectivity exists across the mountain and extends to the south of the typhoon center. Furthermore, these characteristics were observed in many typhoons with cyclonic deflection tracks near Taiwan (Hsu et al., 2018).

3.2. Potential Vorticity Tendency Diagnosis Results

Plenty of westward cyclonic deflection track typhoons deflect toward the left-hand side of TC moving direction (deflect to the southwest) before landfalling Taiwan. To analyze the entire stages of looping motion, three 6-hourly periods are chosen to obtain the PV tendency diagnosis according to simulated track characteristics (Figure 3b). The sequential PV tendency terms every 12 min are averaged for 6 h for temporal smoothing. In the first period, TC moves toward the northwest before cyclonic track deflection (hereafter,
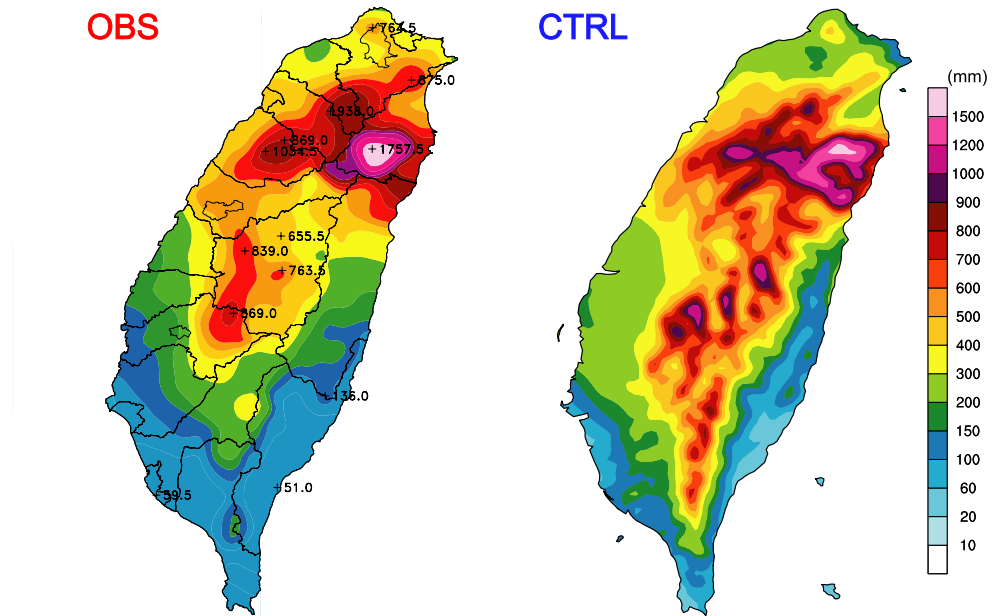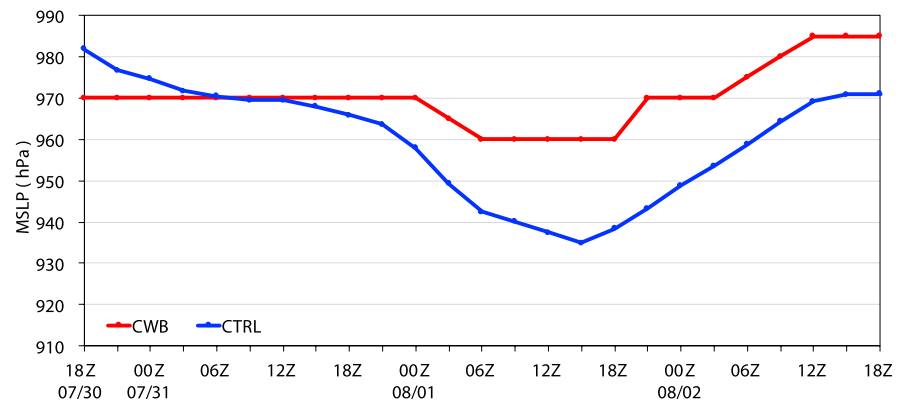
Figure 4. (a) Seventy two hour accumulated rainfall from 18 UTC on 30 July to 18 UTC on 02 August of Weather Research and Forecasting (WRF) control experiment (right) and observation rainfall (left) from Central Weather Bureau (CWB), WRA stations, and rain gauge data (totally 567 stations). (b) 3-hourly minimum sea-level pressure from WRF control experiment (blue) and CWB best track data (red).

stage 1). In the second period, TC experiences a cyclonic track deflection toward the southwest near Taiwan (hereafter, stage 2). Furthermore, this period is the first half of the looping motion in our simulation. In the third period, TC moves toward the north after the cyclonic track deflection near Taiwan (hereafter, stage 3), which is also the last half of the looping motion. The vortex following averaged rainfall rate and symmetric PV component during the three stages are shown in Figures 7a–7c, respectively. The rainfall maximum occurs on the left-hand side of the TC track in stage 1 (Figure 7a). The rainfall maximum becomes significant on the right-hand side of the TC track during stage 2 (Figure 7b). In stage 3, the convection asymmetry begins to weaken, and massive rainfall is located at the left-hand side of the TC motion (Figure 7c).

Figure 7 also shows the PV tendency diagnosis results in three stages with the TC motion vectors contributed by $(HA)_1$ (blue), $(VA)_1$ (green), $(DH)_1$ (red), and total $((HA + VA + DH)_1$, gray) PV tendencies. The TC translation speed (black) was calculated using the linear direction between the first and last TC centers during the target period. Overall, the TC motions contributed by total WN1 PV tendencies represent the
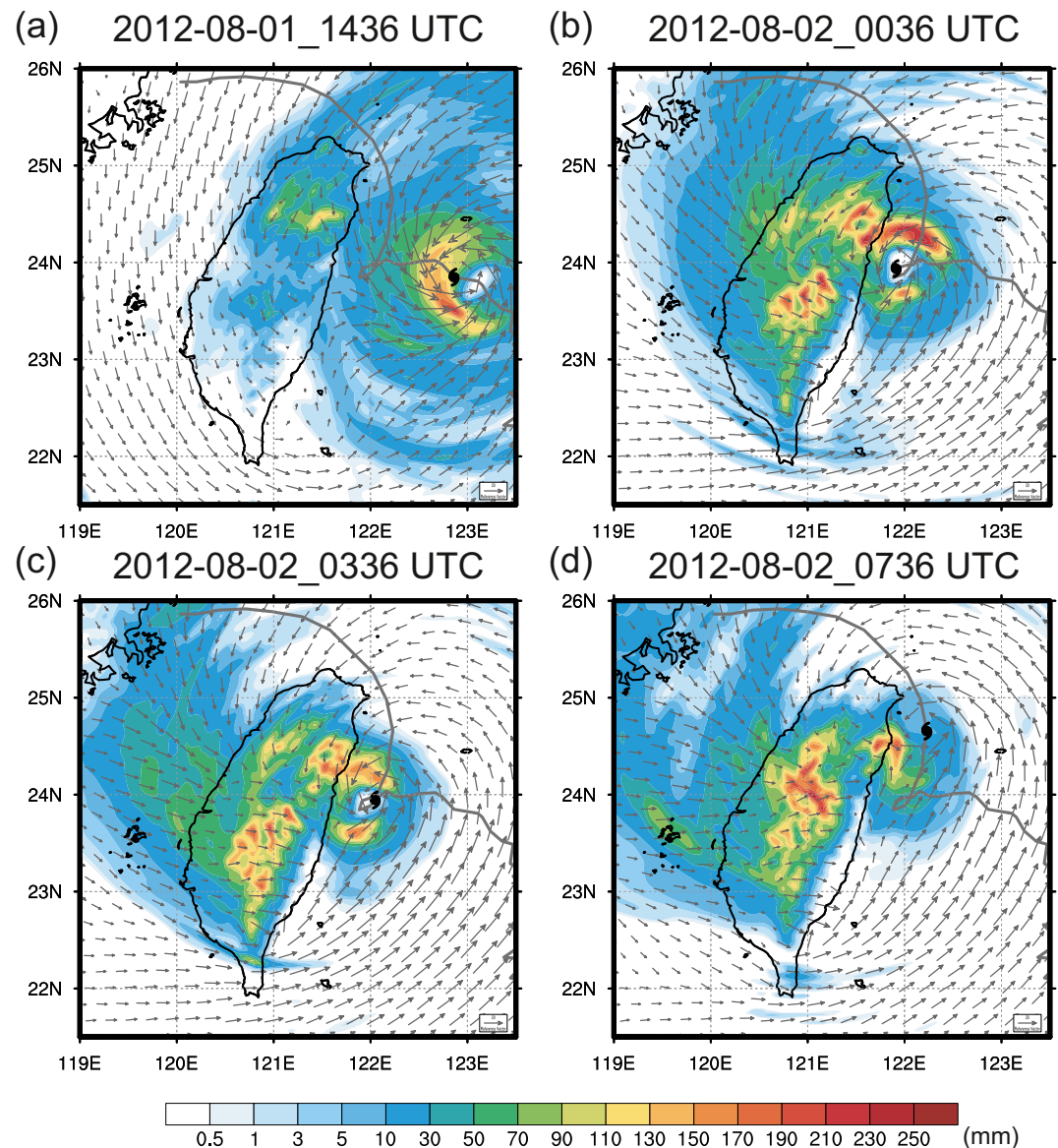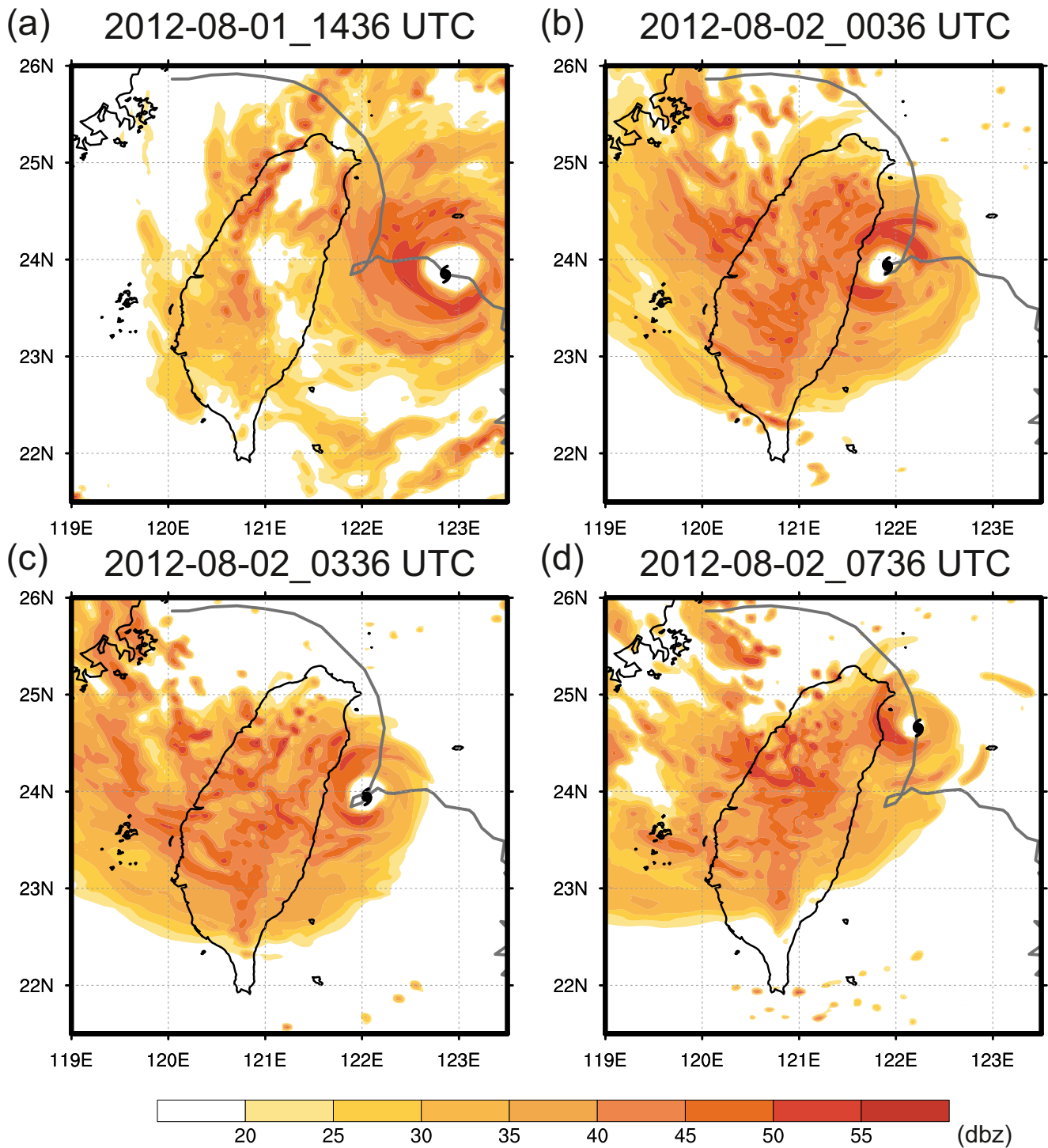
Figure 5. Weather Research and Forecasting-simulated 3-hourly rainfall and 10-m winds at (a) 1436 UTC on August 01, (b) 0036 UTC on August 02, (c) 0336 UTC on August 02, and (d) 0736 UTC on August 02.

simulated TC motions well among three stages. The residuals are relatively small compared to the TC moving vectors (see Figures 10c and 10f for the detailed residual analysis). In stage 1, the TC motion (black vector, Figure 7a) is in agreement with the total PV tendency (gray vector, Figure 7a) in both direction and magnitude. The $(HA)_1$ component is -4.40 and 2.77 m s^{-1} in x and y directions and is pointing to the northwest. The $(VA)_1$ component is 0.72 and -1.23 m s^{-1} in x and y directions and provides the opposite effect to the $(HA)_1$ term. The $(DH)_1$ component is relatively small in this period. The TC motion is mainly contributed by the $(HA)_1$ effect, which is dominated by the steering flow.

The asymmetric convection becomes more significant in stage 2. High rainfall areas are concentrated in the north of the TC center and also in the windward side of northeastern Taiwan (Figure 7b). The $(HA)_1$ term remains pointing to the northwest but becomes smaller (-2.40, 1.34 m s^{-1} in x and y directions) than in stage 1. The $(VA)_1$ term is -0.61 and -0.70 m s^{-1} in x and y directions and points to the southwest. The DH term becomes significant in stage 2, which is 0.23 and -1.70 m s^{-1} in x and y directions and pointing to the south. The $(DH)_1$ and $(VA)_1$ effects contribute to the cyclonic deflection motion in this period. Our results

Figure 6. Weather Research and Forecasting-simulated maximum radar reflectivity (dBZ) within vertical column at (a) 1436 UTC on August 01, (b) 0036 UTC on August 02, (c) 0336 UTC on August 02, and (d) 0736 UTC on August 02.

are in agreement with those reported by Hsu et al. (2013, 2018). Shallower convection developed from the bottom to approximately 4-km in height and is located at approximately 30–40 km east of the center. This shallow convection provides negative heating in most of the troposphere compared with the relatively weak convection in the south and east of the TC (not shown). In the end, this asymmetric heating structure in the north of the TC leads to negative/positive DH WN1 structure in the north/south of the TC.
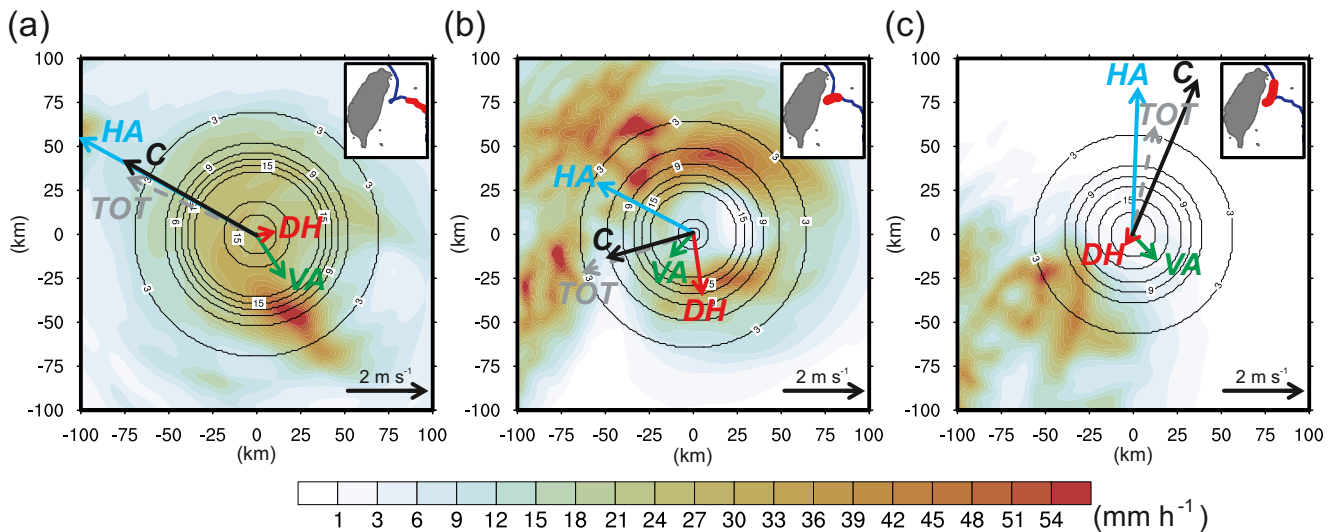
Figure 7. Vortex-following composite fields of rainfall rate (shadings), vertical averaged symmetric PV [PVU] (contours) and the PV tendency diagnosis tropical cyclone (TC) motion vectors in three time periods. (a) 1000 UTC on August 01 to 1600 UTC on August 01, stage 1. (b) 1812 UTC on August 01 to 0012 UTC on August 02, stage 2. (c) 0136 UTC on August 02 to 0736 UTC on August 02, stage 3. The corresponded tracks are denoted as red in the up-right corners of each panel. The symmetric PV and WN1 PV tendency terms are averaged through 6-h and from 600-m to 10-km height within a 40,000 km^2 square area centered on the TC. The vectors represent the TC motion contributed by WN1 of HA (blue), VA (green), DH (red), and total (gray) PV tendencies. Vector C (black) represents the TC moving vector obtained by the TC centers.

The TC moves toward the north in stage 3. The significant asymmetric convection in stage 2 disappeared. The larger rainfall area is located to the southwest of TC; however, it does not coincide with the area where the large symmetric PV gradient exists (Figure 7c). The TC motion is mainly contributed by (HA)$_1$ (0.14, 3.95 m s^{-1} in x and y directions), whereas the WN1 of DH and VA terms are small during stage 3. We further examined the time evolution of the area (24–24.7°N, 121.7–122.7°E) and vertically averaged horizontal winds in lower levels (0–5.6 km) at the north of the TC (Figure 11, blue). The wind directions are in general northeast during stage 1. The east wind components increase steadily in stage 2 and cause the rainfall maxima in the windward side of northern Taiwan. After the cyclonic deflection motion, the easterly wind component decreases rapidly. The circulation may be altered by topography, and the southerly wind component becomes dominant during stage 3. Therefore, the convection in the windward side becomes insignificant and reduces the WN1 asymmetries of DH distribution. Furthermore, the enhanced south wind may increase the (HA)$_1$ effect point toward the north during stage 3.

4. Sensitivities of TC Tracks to Cloud Microphysics

Because the looping track near the terrain is caused by convection, sensitivity experiments with different cloud microphysics schemes are performed. The purpose of these experiments is to study the effect of convection distribution on typhoon motion. Figure 8 shows the simulated typhoon tracks of CTRL and experiments with Thompson (THOM, light blue), Lin (LIN, black), WSM6 (WSM6, gray), Morrison (MORR, green), and WDM6 (WDM6, light green) schemes. Among all experiments, CTRL, THOM, LIN, and WSM6 show cyclonic deflection tracks while TC is approaching. In addition, WSM6-run makes landfall after the cyclonic deflection, whereas the other three experiments move toward the north. By contrast, MORR and WDM6 move nearly straight.

Figures 9a–9f shows the 6-hourly accumulated rainfall during stage 2. The blue crosses denote the TC centers during this period. Similar simulated hours in WDM6 and MORR runs (Figures 9b and 9c) are chosen for comparison because no cyclonic deflection tracks occur in these two experiments. An asymmetric larger rainfall area is located north of the typhoon in CTRL, THOM, LIN, and WSM6 experiments. Otherwise, MORR and WDM6 runs do not have significant convections at the windward side of topography. Figures 9g–9i further examine the rainfall distribution of CTRL, THOM, and LIN experiments in stage 3.
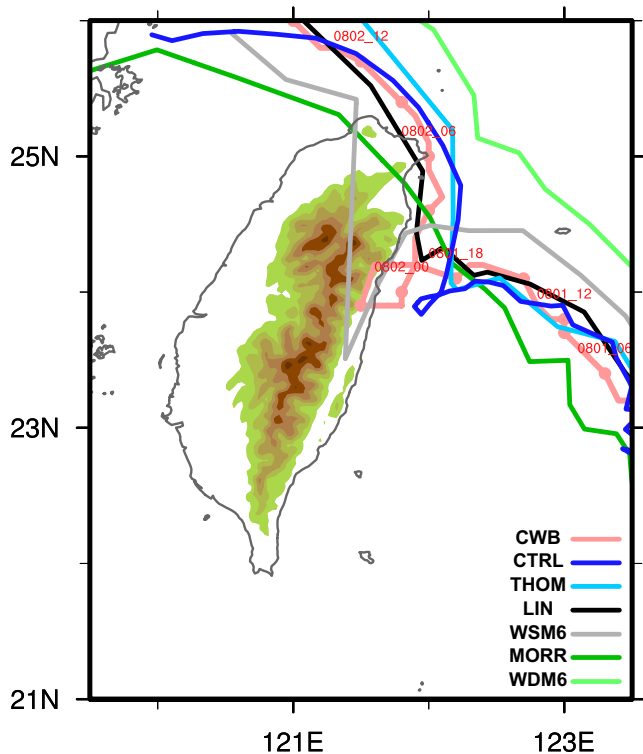
Figure 8. Simulated tracks of Typhoon Saola (2012) for the microphysics sensitivity experiments. The red line is Central Weather Bureau's best track. The blue line is the hourly track of control experiment with Goddard microphysics. Gray, black, light green, green, and light blue lines represent the experiments with WSM6, Lin, WDM6, Morrison, and Thompson microphysics, respectively. Three-hourly tracks of microphysics sensitivity experiments are plotted for simplicity.

The rainfall north of TC becomes weak, while the local rainfall maximum appears to the left-hand side of TC motion, which is located on the northeastern coast of Taiwan.

Figures 10a and 10b show that the WN1 PV tendency diagnosis results from $(HA)_1$ and the contributions from $(DH)_1$ plus $(VA)_1$ PV tendency terms $(DH + VA)_1$ in stage 2 for all sensitivity experiments, respectively. All the HA PV tendencies contribute to the northwestward TC motions and all the $(DH + VA)_1$ terms pointing to the south. For the experiments with apparently cyclonic deflection tracks and asymmetric convection distribution, the HA term is smaller, and $(DH + VA)_1$ is larger. CTRL and WSM6 experiments have the most significant southward typhoon motion components in $(DH + VA)_1$, followed by LIN and THOM, and the last two are WDM6 and MORR. The results reveal that the cyclonic deflection tracks in our experiments are associated with the asymmetric convection distribution and modify the TC looping southward motion through $(DH + VA)_1$ PV tendencies. The model cloud microphysics are sensitive in producing asymmetric convection. Figures 10d and 10e show the PV tendency analysis in stage 3 for CTRL, THOM, and LIN experiments. The results show that $(DH + VA)_1$ is smaller compared with $(HA)_1$. The $(HA)_1$ effect dominates the TC motion and points to the north in this period. Figures 10c and 10f show the normalized differences between the total PV tendencies $(HA + VA + DH)_1$ and the simulated TC motion vectors. The normalization was done by scaling to the TC motion vectors. The residual terms may increase while the storm translation speed increased in stage 3. However, Figures 10c and 10f show that the residual terms in our analysis are relatively small, and the total PV tendencies are acceptable to represent the simulated storm motion.

The time evolution area-averaged lower-level winds of THOM (light blue) and LIN (black) are similar to CTRL (blue) (Figure 11). Both experiments showed that significant easterlies exist on the windward side near the eastern coast of Taiwan during stage 2. The easterlies start to weaken and veer to southerly in stage 3. The aforementioned procedure is consistent with CTRL and reveals that the $(HA)_1$ effect becomes important due to the change in wind direction north of the typhoon during stage 3. After that, the intensified westerlies show that the TC was passing through the analysis box and moves to the north.

## 5. Conclusions and Discussions

Typhoon track deflections often occurred in the northern part of Taiwan's east coast before making landfall. Most of the deflected storms occurred with strong intensity (e.g., Hsu et al., 2018). Previous model studies suggest that the strong vortex interacted with the topography favor the occurrence of southward deflection track or looping track. These studies highlight the importance of the channeling effect that lead to the deflected southward movement. Typhoon Saola (2012), with a weak intensity of Cat. 1, experience a cyclonic looping motion for 12 h while approaching the northeastern coast of Taiwan. The WRF model simulated well the looping track of Typhoon Saola (2012). The PV tendency diagnosis analysis is conducted to study the processes of the model's looping track. The residual term in the PV tendency diagnosis is very small and thus rendering the validity of the PV tendency analysis to the looping track.

Three stages, before cyclonic deflection (stage 1), during cyclonic deflection and looping (stage 2), and after cyclonic deflection (stage 3), are defined. Stages 2 and 3 constitute the looping period studied in the present paper. In stage 1, the TC is far from Taiwan and moves toward the northwest. The TC motion is dominated by the steering flow, which relates to the HA term contribution in the PV tendency analysis. The TC moved southwestward in the looping track during stage 2. The rainfall to the north on the windward side of the
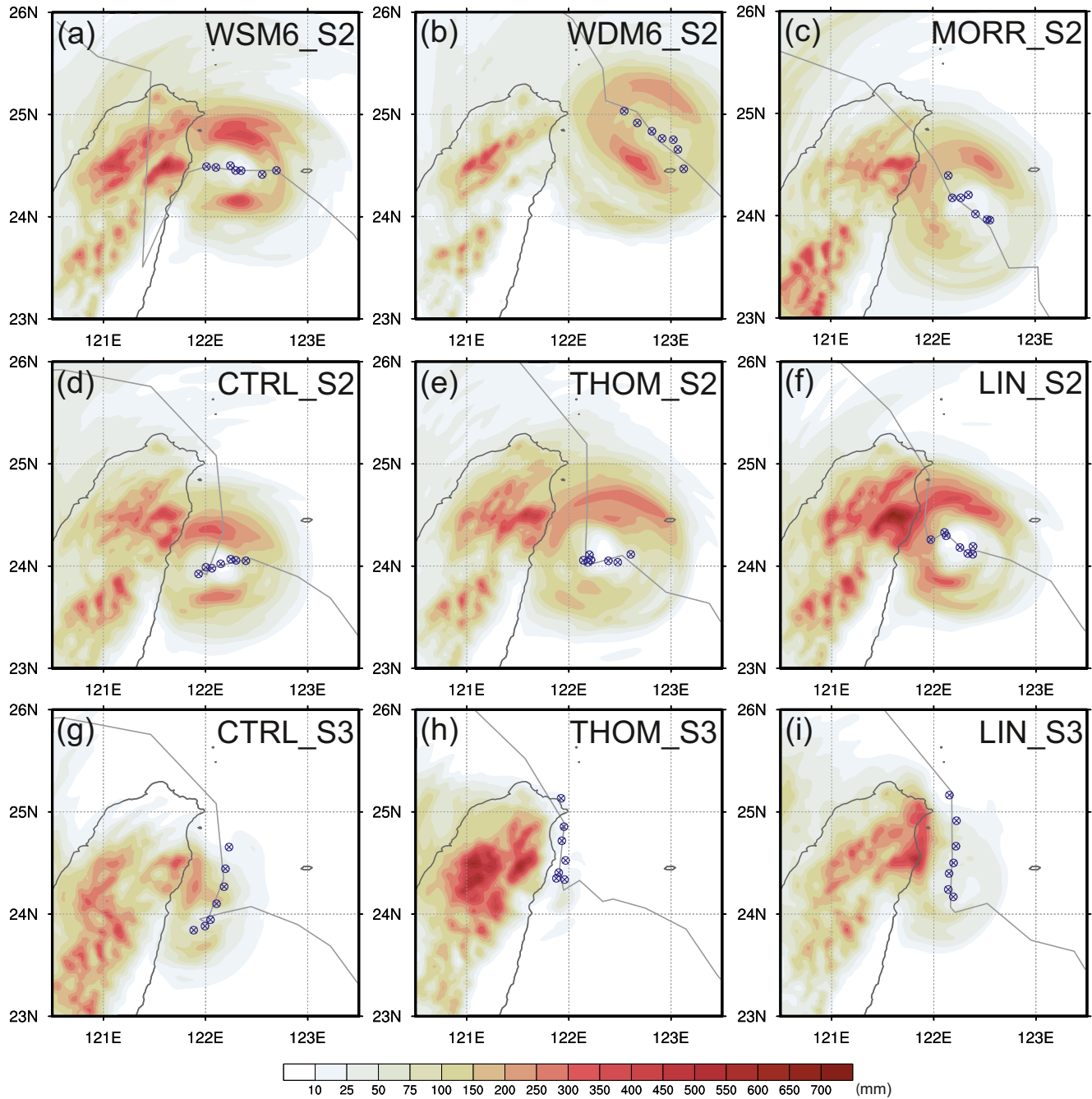
Figure 9. The 6-h accumulated rainfall with typhoon centers (blue cross) during stage 2 of (a) WSM6, (b) WDM6, (c) MORR, (d) CTRL, (e) THOM, and (f) LIN experiments. Similar model periods are chosen for MORR and WDM6 experiments for comparison. (g–i) show the 6-h accumulated rainfall during stage 3 of CTRL, THOM, and LIN experiments, respectively.

typhoon at this stage is significant. The convection, however, is with a peak heating at a relatively low altitude below 500 hPa and the vertical averaged PV DH tendency is negative. To the south of the storm, the convection is weak due to the downslope wind and the vertically averaged DH tendency is near zero. Thus, the WN1 DH tendency is southward. In addition, a vertical stretching of PV is observed in the downslope wind to the south of the storm. The downslope wind constitutes the WN1 VA tendency toward the south. These asymmetric patterns of VA and DH contribute to the southward positive PV tendency and lead to the cyclonic deflection southward motion during stage 2. In agreement with the weak intensity of Typhoon Saola, our model analysis did not support the role of the channeling effect on the southward motion of
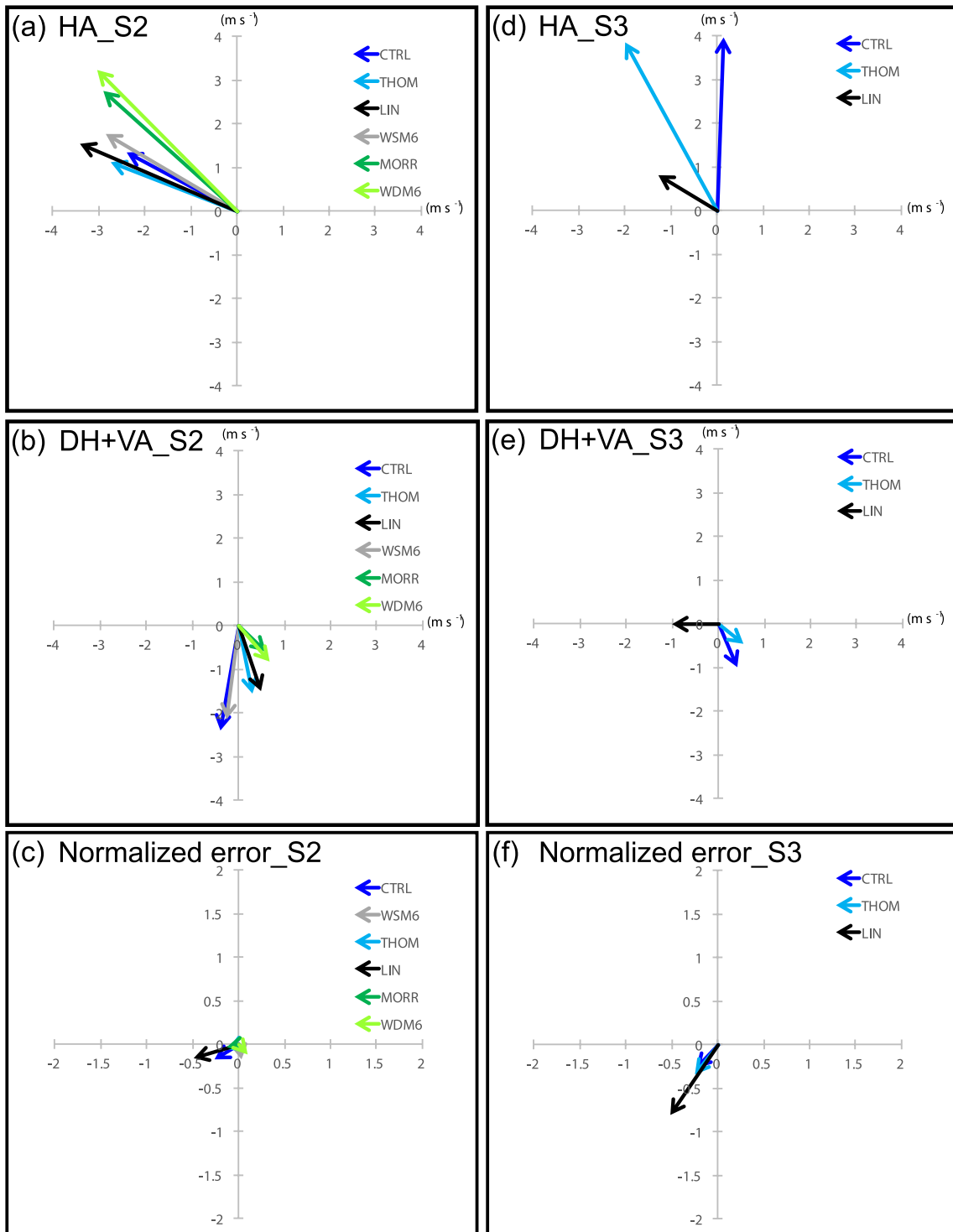
Figure 10. PV tendency diagnosis of different microphysics sensitivity experiments during stages 2 (a–c) and 3 (d–f). (a, d) HA component. (b, e) DH plus VA components. (c, f) Normalized differences between the total PV tendencies $(HA + VA + DH)_1$ and the simulated tropical cyclone (TC) motion vectors. Normalization was done by dividing the TC motion vectors. Blue, light blue, black, gray, green, and light green vectors represent the results of CTRL, THOM, LIN, WSM6, MORR, WDM6, respectively.
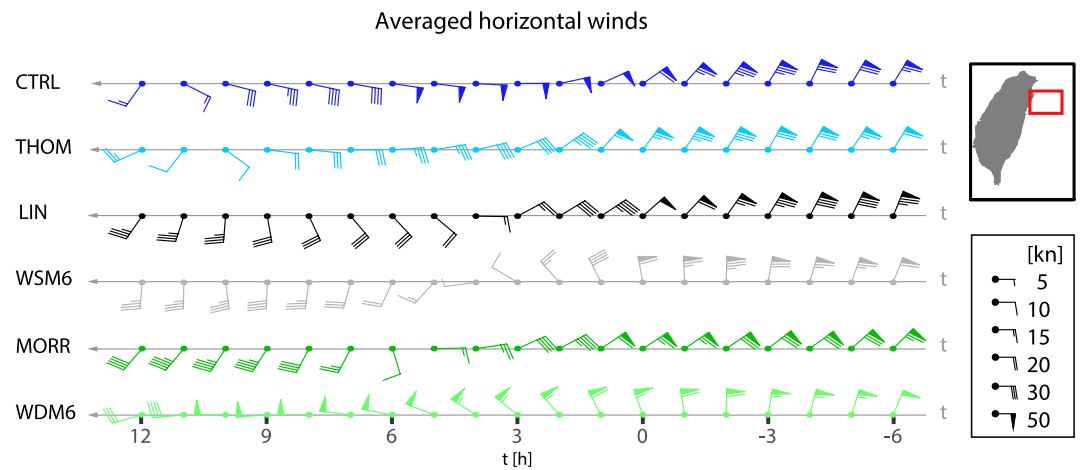
Figure 11. The time evolution of averaged horizontal winds over 0–5.6 km altitude and in the area of 24–24.7°N, 121.7–122.7°E for six microphysics sensitivity experiments.

the looping track. Our model result suggests that at stage 3, the easterly wind component decreases while the southerly wind component becomes dominant in offshore northeastern Taiwan. The convections, in general, become weaker to the north of the TC in stage 3, and the WN1 DH becomes weak. Moreover, the downslope wind is weakened when the storm moves southward and the flow is more difficult to cross the CMR. The DH and VA effects become insignificant during stage 3, and the WN1 HA effect leads the TC to move northward in stage 3. Stage 2 cyclonic deflection and stage 3 northwestward motion constitute a 12-h looping motion, which causes heavy precipitation in the northeast of the Taiwan area.

Our numerical experiments show that the WN1 diabatic convection process (DH + VA) affects the typhoon path near the terrain in the northeast of Taiwan. The experiments show that TC's looping track simulation is sensitive to the choices of model cloud microphysics schemes. The model sensitivity study indicates that a large part of track uncertainty resides in the interaction of model internal dynamics and model cloud microphysics. Our cloud microphysics sensitivity tests show that the track uncertainty can increase dramatically from 48 to 140 km during 00 UTC August 01 to 00 UTC August 02. This variation of TC track (w/ wo landfall) within 24-h could cause the landfall position shift from Yilan to Hualien County in Taiwan, which results in a different topographic phase-locking rainfall distribution and also rainfall duration (Cheung et al., 2008; Hsu et al., 2013). The magnitude of the track uncertainty is in general comparable to that of Fovell et al. (2010), which a span of 115 km track variations in 72 h can be produced by using different microphysics schemes.

Our experiments with a single-moment type of microphysics simulate the looping track well and the double-moment experiments fail to simulate the looping track. Since DH PV tendency is very important in the southward movement of the looping track, it indicates that the microphysics affect the vertical diabatic heating profile and the PV generation. The tendency of the number concentration and size parameter was forced to be synchronized in single-moment microphysics. But, the tendency of these two parameters can be in the different phases within the double-moment microphysics. Namely, it may be caused by the different time-scale of diabatic heating process efficiency in these microphysics schemes. The detail of the microphysics analysis remains to be the challenge. Further experiments and diabatic budget analysis should be conducted in the future. In recent years, more and more state-of-the-art radar data and techniques are established in Taiwan. Radar reflectivity, radial wind, and even polarimetric variables, such as differential reflectivity (ZDR), specific differential phase shift (KDP), and so on, can retrieval the high spatial-temporal resolution of the hydrometers and dynamic structures in typhoons. These high-resolution data and numerical experiments may help to improve our understanding of microphysics in the looping track predictions.

Data Availability Statement

Those observation data can be accessed via the DBAR (https://dbar.pccu.edu.tw/) and CWB (https://www.cwb.gov.tw/eng/). This manuscript was edited by Wallace Academic Editing.

References

Cao, Y., Fovell, R. G., & Corbosiero, K. L. (2011). Tropical cyclone track and structure sensitivity to initialization in idealized simulations: A preliminary study. *Terrestrial, Atmospheric and Oceanic Sciences*, *22*, 559–578. https://doi.org/10.3319/TAO.2011.05.12.01(TM)

Chen, S.-H., & Sun, W.-Y. (2002). A one-dimensional time dependent cloud model. *Journal of the Meteorological Society of Japan*, *80*(1), 99–118. https://doi.org/10.2151/jmsj.80.99

Chen, Y.-H., Kuo, H.-C., Wang, C.-C., & Yang, Y.-T. (2017). Influence of southwest monsoon flow and typhoon track on Taiwan rainfall during the exit phase: Modelling study of typhoon Morakot (2009). *Quarterly Journal of the Royal Meteorological Society*, *143*, 3014–3024. https://doi.org/10.1002/qj.3156

Cheung, K. K. W., Huang, L.-R., & Lee, C.-S. (2008). Characteristics of rainfall during tropical cyclone periods in Taiwan. *Natural Hazards and Earth System Sciences*, *8*, 1463–1474. https://doi.org/10.5194/nhess-8-1463-2008

Danielson, J. J., & Gesch, D. B. (2011). *Global multi-resolution terrain elevation data 2010 (GMTED2010), Open-File Report 2011–1073*. U.S. Geological Survey.

Fovell, R. G., Bu, Y. P., Corbosiero, K. L., Tung, W.-W., Cao, Y., Kuo, H.-C., et al. (2016). Influence of cloud microphysics and radiation on tropical cyclone structure and motion. In *Multiscale convection-coupled systems in the tropics: A tribute to Dr. Michio Yanai, Meteor. Monogr., No. 56* (pp. 11.1–11.27). Amer. Meteor. Soc. https://doi.org/10.1175/AMSMONOGRAPHS-D-15-0006.1

Fovell, R. G., Corbosiero, K. L., & Kuo, H. C. (2009). Cloud microphysics impact on hurricane track as revealed in idealized experiments. *Journal of the Atmospheric Sciences*, *66*, 1764–1778. https://doi.org/10.1175/2008JAS2874.1.10.1175/2008jas2874.1

Fovell, R. G., Corbosiero, K. L., Seifert, A., & Liou, K.-N. (2010). Impact of cloud-radiative processes on hurricane track. *Geophysical Research Letters*, *37*, L07808. https://doi.org/10.1029/2010GL042691

Fovell, R. G., & Su, H. (2007). Impact of cloud microphysics on hurricane track forecasts. *Geophysical Research Letters*, *34*, L24810. https://doi.org/10.1029/2007GL031723

Friedl, M. A., Sulla-Menashe, D., Tan, B., Schneider, A., Ramankutty, N., Sibley, A., & Huang, X. (2010). MODIS Collection 5 global land cover: Algorithm refinements and characterization of new datasets. *Remote Sensing of Environment*, *114*, 168–182. https://doi.org/10.1016/j.rse.2009.08.016

Hong, S.-Y., & Lim, J.-O. J. (2006). The WRF single–moment 6–class microphysics scheme (WSM6). *Journal of the Korean Meteorological Society*, *42*, 129–151.

Hong, S.-Y., Noh, Y., & Dudhia, J. (2006). A new vertical diffusion package with an explicit treatment of entrainment processes. *Monthly Weather Review*, *134*, 2318–2341. https://doi.org/10.1175/MWR3199.1

Hsu, L.-H., Kuo, H.-C., & Fovell, R. G. (2013). On the geographic asymmetry of typhoon translation speed across the mountainous island of Taiwan. *Journal of the Atmospheric Sciences*, *70*, 1006–1022. https://doi.org/10.1175/jas-d-12-0173.1

Hsu, L.-H., Su, S.-H., Fovell, R. G., & Kuo, H.-C. (2018). On typhoon track deflections near the east coast of Taiwan. *Monthly Weather Review*, *146*, 1495–1510. https://doi.org/10.1175/MWR-D-17-0208.1

Huang, C.-Y., & Lin, Y.-L. (2008). The influence of mesoscale mountains on vortex tracks: Shallow-water modeling study. *Meteorology and Atmospheric Physics*, *101*, 1–20. https://doi.org/10.1007/s00703-007-0284-1

Huang, C.-Y., Zhang, Y., Skamarock, W. C., & Hsu, L.-H. (2017). Influences of large-scale flow variations on the track evolution of Typhoons Morakot (2009) and Megi (2010): Simulations with a global variable-resolution model. *Monthly Weather Review*, *145*, 1691–1716. https://doi.org/10.1175/MWR-D-16-0363.1

Huang, Y.-C., & Lin, Y.-L. (2018). Looping tracks associated with tropical cyclones approaching an isolated mountain. Part I: Essential parameters. *Meteorology and Atmospheric Physics*, *130*, 333–348. https://doi.org/10.1007/s00703-017-0533-x

Huang, Y.-H., Wu, C.-C., & Wang, Y. (2011). The influence of island topography on typhoon track deflection. *Monthly Weather Review*, *139*, 1708–1727. https://doi.org/10.1175/2011MWR3560.1

Iacono, M. J., Delamere, J. S., Mlawer, E. J., Shephard, M. W., Clough, S. A., & Collins, W. D. (2008). Radiative forcing by long–lived greenhouse gases: Calculations with the AER radiative transfer models. *Journal of Geophysical Research*, *113*, D13103. https://doi.org/10.1029/2008JD009944

Jian, G.-J., & Wu, C.-C. (2008). A numerical study of the track deflection of Super-typhoon Haitang (2005) prior to its landfall in Taiwan. *Monthly Weather Review*, *136*, 598–615. https://doi.org/10.1175/2007MWR2134.1

Jimenez, P. A., Dudhia, J., Gonzalez–Rouco, J. F., Navarro, J., Montavez, J. P., & Garcia–Bustamante, E. (2012). A revised scheme for the WRF surface layer formulation. *Monthly Weather Review*, *140*, 898–918. https://doi.org/10.1175/MWR-D-11-00056.1

Kuo, H.-C., Williams, R. T., Chen, J.-H., & Chen, Y.-L. (2001). Topographic effects on barotropic vortex motion: No mean flow. *Journal of the Atmospheric Sciences*, *58*, 1310–1327. https://doi.org/10.1175/1520-0469(2001)058,1310:TEOBVM.2.0.CO;2

Lim, K.-S. S., & Hong, S.-Y. (2010). Development of an effective double–moment cloud microphysics scheme with prognostic cloud condensation nuclei (CCN) for weather and climate models. *Monthly Weather Review*, *138*, 1587–1612. https://doi.org/10.1175/2009MWR2968.1

Lin, Y.-L., Chen, S.-H., & Liu, L. (2016). Orographic influence on basic flow and cyclone circulation and their impacts on track deflection of an idealized tropical cyclone. *Journal of the Atmospheric Sciences*, *73*, 3951–3974. https://doi.org/10.1175/JAS-D-15-0252.1

Lin, Y.-L., Chen, S.-Y., Hill, C. M., & Huang, C.-Y. (2005). Control parameters for the influence of a mesoscale mountain range on cyclone track continuity and deflection. *Journal of the Atmospheric Sciences*, *62*, 1849–1866. https://doi.org/10.1175/JAS3439.1

Lin, Y.-L., Han, J., Hamilton, D. W., & Huang, C.-Y. (1999). Orographic influence on a drifting cyclone. *Journal of the Atmospheric Sciences*, *56*, 534–562. https://doi.org/10.1175/1520-0469(1999)056,0534:OIOADC.2.0.CO;2

Lin, Y.-L., & Savage, L. C., III (2011). Effects of landfall location and the approach angle of a cyclone vortex encountering a mesoscale mountain range. *Journal of the Atmospheric Sciences*, *68*, 2095–2106. https://doi.org/10.1175/2011JAS3720.1

Liu, L., Lin, Y.-L., & Chen, S.-H. (2016). Effects of landfall location and approach angle of an idealized tropical cyclone over a long mountain range. *Frontiers of Earth Science*, *4*, 14. https://doi.org/10.3389/feart.2016.00014

Morrison, H., Thompson, G., & Tatarskii, V. (2009). Impact of cloud microphysics on the development of trailing stratiform precipitation in a simulated squall line: Comparison of one- and two-moment schemes. *Monthly Weather Review*, *137*, 991–1007. https://doi.org/10.1175/2008MWR2556.1

National Centers for Environmental Prediction/National Weather Service/NOAA/U. S. Department of Commerce (NCEP). (2000). NCEP FNL operational model global tropospheric analyses, continuing from July 1999. In *Research data archive at the National Center for Atmospheric Research*. Computational and Information Systems Laboratory. https://doi.org/10.5065/D6M043C6

Skamarock, W. C., Klemp, J. B., Dudhia, J., Gill, D. O., Barker, D. M., Duda, M. G., et al. (2008). *A description of the advanced research WRF version 3*. (NCAR Tech). Note NCAR/TN-475+STR, 113 pp. https://doi.org/10.5065/D68S4MVH

Su, S.-H., Kuo, H.-C., Hsu, L.-H., & Yang, Y.-T. (2012). Temporal and spatial characteristics of typhoon extreme rainfall in Taiwan. *Journal of the Meteorological Society of Japan*, *90*, 721–736. https://doi.org/10.2151/jmsj.2012-510

Tang, C. K., & Chan, J. C. L. (2014). Idealized simulations of the effect of Taiwan and Philippines topographies on tropical cyclone tracks. *Quarterly Journal of the Royal Meteorological Society*, *140*, 1578–1589. https://doi.org/10.1002/qj.2240

Tang, C. K., & Chan, J. C. L. (2015). Idealized simulations of the effect of local and remote topographies on tropical cyclone tracks. *Quarterly Journal of the Royal Meteorological Society*, *141*, 2045–2056. https://doi.org/10.1002/qj.2498

Tang, C. K., & Chan, J. C. L. (2016). Idealized simulations of the effect of Taiwan topography on the tracks of tropical cyclones with different steering flow strengths. *Quarterly Journal of the Royal Meteorological Society*, *142*, 3211–3221. https://doi.org/10.1002/qj.2902

Tao, W.-K., Simpson, J., & McCumber, M. (1989). An ice–water saturation adjustment. *Monthly Weather Review*, *117*, 231–235. https://doi.org/10.1175/1520-0493(1989)117<0231:AIWSA>2.0.CO;2

Tao, W.-K., Wu, D., Lang, S., Chern, J.-D., Peters-Lidard, C., Fridlind, A., & Matsui, T. (2016). High-resolution NU-WRF simulations of a deep convective-precipitation system during MC3E: Further improvements and comparisons between Goddard microphysics schemes and observations. *Journal of Geophysical Research: Atmospheres*, *121*, 1278–1305. https://doi.org/10.1002/2015JD023986

Tewari, M., Chen, F., Wang, W., Dudhia, J., LeMone, M. A., Mitchell, K., et al. (2004). Implementation and verification of the unified NOAH land surface model in the WRF model. In *20th Conference on Weather Analysis and Forecasting/16th Conference on Numerical Weather Prediction* (pp. 11–15).

Thompson, G., Field, P. R., Rasmussen, R. M., & Hall, W. D. (2008). Explicit forecasts of winter precipitation using an improved bulk microphysics scheme. Part II: Implementation of a new snow parameterization. *Monthly Weather Review*, *136*, 5095–5115. https://doi.org/10.1175/2008MWR2387.1

Wang, C.-C., Chen, Y.-H., Kuo, H.-C., & Huang, S.-Y. (2013). Sensitivity of typhoon track to asymmetric latent heating/rainfall induced by Taiwan topography: A numerical study of Typhoon Fanapi (2010). *Journal of Geophysical Research: Atmospheres*, *118*, 3292–3308. https://doi.org/10.1002/jgrd.50351

Wang, C.-C., Kuo, H.-C., Chen, Y.-H., Huang, H.-L., Chung, C.-H., & Tsuboki, K. (2012). Effects of asymmetric latent heating on typhoon movement crossing Taiwan: The case of Morakot (2009) with extreme rainfall. *Journal of the Atmospheric Sciences*, *69*, 3172–3196. https://doi.org/10.1175/JAS-D-11-0346.1

Wu, C.-C., Li, T.-H., & Huang, Y.-H. (2015). Influence of mesoscale topography on tropical cyclone tracks: Further examination of the channeling effect. *Journal of the Atmospheric Sciences*, *72*, 3032–3050. https://doi.org/10.1175/JAS-D-14-0168.1

Wu, L., & Wang, B. (2000). A potential vorticity tendency di- agnostic approach for tropical cyclone motion. *Monthly Weather Review*, *128*, 1899–1911. https://doi.org/10.1175/1520-0493(2000)128,1899:APVTDA.2.0.CO;2

Wu, L., & Wang, B. (2001). Effects of convective heating on movement and vertical coupling of tropical cyclones: A numerical study. *Journal of the Atmospheric Sciences*, *58*, 3639–3649. https://doi.org/10.1175/1520-0469(2001)058,3639:EOCHOM.2.0.CO;2

Yeh, T.-C., & Elsberry, R. L. (1993). Interaction of typhoons with the Taiwan orography. Part I: Upstream track deflections. *Monthly Weather Review*, *121*, 3193–3212. https://doi.org/10.1175/1520-0493(1993)121,3193:IOTWTT.2.0.CO;2

Yeh, T.-C., Hsiao, L.-F., Chen, D.-S., & Huang, K.-N. (2012). A study on terrain induced tropical cyclone looping in East Taiwan: Case study of Typhoon Haitang in 2005. *Natural Hazards*, *63*(3), 1497–1514. https://doi.org/10.1007/s11069-011-9876-7